

Atomistic modeling of the metallic-to-semiconducting phase boundaries in monolayer MoS₂

Dipankar Saha and Santanu Mahapatra

Citation: [Applied Physics Letters](#) **108**, 253106 (2016); doi: 10.1063/1.4954257

View online: <http://dx.doi.org/10.1063/1.4954257>

View Table of Contents: <http://scitation.aip.org/content/aip/journal/apl/108/25?ver=pdfcov>

Published by the [AIP Publishing](#)

Articles you may be interested in

[Bonding between graphene and MoS₂ monolayers without and with Li intercalation](#)

Appl. Phys. Lett. **107**, 043903 (2015); 10.1063/1.4927611

[Adsorption of alkali, alkaline-earth, simple and 3d transition metal, and nonmetal atoms on monolayer MoS₂](#)

AIP Advances **5**, 057143 (2015); 10.1063/1.4921564

[Atomistic simulation of the electronic states of adatoms in monolayer MoS₂](#)

Appl. Phys. Lett. **104**, 141603 (2014); 10.1063/1.4870767

[On the mobility and contact resistance evaluation for transistors based on MoS₂ or two-dimensional semiconducting atomic crystals](#)

Appl. Phys. Lett. **104**, 113504 (2014); 10.1063/1.4868536

[High-performance MoS₂ transistors with low-resistance molybdenum contacts](#)

Appl. Phys. Lett. **104**, 093106 (2014); 10.1063/1.4866340

The advertisement for MMR Technologies features a blue and white background with a grid pattern. On the left is the MMR Technologies logo, which consists of a stylized 'M' and 'R' in a blue and red arc, with 'TECHNOLOGIES' written below. To the right of the logo is the text 'THE WORLD'S RESOURCE FOR VARIABLE TEMPERATURE SOLID STATE CHARACTERIZATION' in bold, black, uppercase letters. Below this text are five images of scientific equipment: 1. Optical Studies Systems, showing a small device and a larger unit. 2. Seebeck Studies Systems, showing a blue unit labeled 'SB1000' and 'K2000'. 3. Microprobe Stations, showing a circular device with multiple probes. 4. Hall Effect Study Systems and Magnets, showing a blue unit labeled 'H5000' and 'K2000' and a large magnet assembly. At the bottom left is the website 'WWW.MMR-TECH.COM' in red. Below each image is a label: 'OPTICAL STUDIES SYSTEMS', 'SEEBECK STUDIES SYSTEMS', 'MICROPROBE STATIONS', and 'HALL EFFECT STUDY SYSTEMS AND MAGNETS'.

Atomistic modeling of the metallic-to-semiconducting phase boundaries in monolayer MoS₂

Dipankar Saha^{a)} and Santanu Mahapatra^{b)}

Nano-Scale Device Research Laboratory, Department of Electronic Systems Engineering, Indian Institute of Science (IISc) Bangalore, Bangalore 560012, India

(Received 15 March 2016; accepted 7 June 2016; published online 20 June 2016)

Recent experimental demonstration on the coexistence of metallic and semiconducting phases in the same monolayer MoS₂ crystal has attracted much attention for its use in ultra-low contact resistance-MoS₂ transistors. However, the electronic structures of the metallic-to-semiconducting phase boundaries, which appear to dictate the carrier injection in such transistors, are not yet well understood. In this letter, interfacing the 2H and 1T' polytypes appropriately, we first model the “beta” (β) and the “gamma” (γ) phase boundaries, and demonstrate good agreement with experiential results. We then apply first-principles based density functional theory to calculate the electronic structures for those optimized geometries. We further employ non equilibrium Green's function formalism to evaluate the transmission spectra and the local density of states (LDOS) in order to assess the Schottky barrier nature of the phase boundaries. Our study reveals that while the γ boundary yields p-type Schottky barrier, the β boundary leads to the distinct symmetric Schottky barrier with an atomically sharp transition region. This understanding could be useful for designing high performance transistors using phase-engineered MoS₂ crystals. *Published by AIP Publishing.* [<http://dx.doi.org/10.1063/1.4954257>]

Atomically thin layered materials have emerged as the alternative to silicon for the realization of decanometer scale solid state digital switches.¹⁻⁶ This is due to their ultra-thin planar structure that promises to offer excellent gate control over the channel of a MOS transistor.¹⁻³ The transition-metal dichalcogenides (TMDs), especially MoS₂, owing to their finite intrinsic bandgap,⁷⁻⁹ appear to be the more suitable choice (than the metallic graphene) for digital logic applications in spite of their inferior carrier mobility.¹⁰ However, in experimental MoS₂ channel based transistor, the drain current is always found much lower than expected.^{1,11} The origin of low drive current is mainly attributed to the formation of Schottky barrier at metal contacts, which suppresses the carrier injection to the channel.^{3,12} Moreover, due to the unavailability of efficient doping techniques for such atomically thin materials, it is difficult to realize purely ohmic, low resistive metal contacts.^{1,12-14} Exploration of several metals^{12,14,15} with different work functions did not provide the desired solution because of the work function-modification by interface dipole formation and production of gap states from Mo d-orbitals.¹⁵ Several innovative techniques, like chemical doping,¹⁶ insertion of graphene¹⁷ and TiO₂,¹⁸ etc., have also been investigated to mitigate the Schottky barrier limited carrier injection.

Recently, Kappera *et al.*¹⁹ proposed a radical approach where metallic 1T phases of MoS₂ are locally induced on semiconducting 2H phase at the source/drain regions. This resulted in substantial reduction of the contact resistance values. They further observed that the change of metal electrodes has limited influence on the transistor performance, suggesting that the properties of phase boundaries dictate carrier

injection into the channel.^{19,20} Lin *et al.*^{21,22} provide some more insights on these phase boundaries. Analyzing the atomic arrangement by annular dark field (ADF)/scanning transmission electron microscope (STEM) images, they observed two different patterns and called them β and γ . In fact, they judge the atomic positions of “Mo” and “S” by comparing the difference in intensities available from the ADF images.^{21,23} However, their study does not include the details of the electronic structures and the transport properties of those metallic-to-semiconducting phase boundaries. This motivated us to develop the atomistic models for those interfaces, which could be useful to understand the electronic properties as well as the carrier transport in phase-engineered MoS₂ flakes.

Now, the phase transition in MoS₂ (form 2H to 1T) itself is a complicated process which largely depends on the electron dose as well as the thermal environment.²¹ The chemical method called “lithium intercalation” is one of the most extensively practiced processes,^{24,25} which increases the density of electrons in d-orbital and promotes phase transition from the 2H MoS₂ to the metallic 1T MoS₂ (by destabilizing the 2H phase).^{25,26} However, the meta-stable 1T phase may further relax to a much lower energy state, simply by redefining its lattice vectors.^{25,27} This distorted 1T MoS₂ is actually the 1T' phase of monolayer MoS₂ (for which the relative energetic stability has greatly improved).

Owing to the fact that the 1T' phase of monolayer MoS₂ replicates nothing but the distorted 1T phase,^{25,27-30} here we use the 1T' and 2H polytypes while modeling the planar hetero-phase structures. The first-principles based density functional theory (DFT) calculations are performed using the software package Atomistix Tool Kit (ATK).³¹ The density functional theory has been employed in conjunction with the generalized gradient approximation (GGA) exchange

^{a)}Electronic mail: dipsah_etc@yahoo.co.in

^{b)}Electronic mail: santanu@dese.iisc.ernet.in

correlation and the Perdew, Burke, and Ernzerhof (PBE) functional.³² Apart from that, we use the OPENMX (Open source package for Material eXplorer) norm-conserving pseudopotentials^{33,34} (as implemented in ATK database), with pseudo-atomic orbitals (PAO) and the “medium” basis sets having the cut-off radius of basis functions ~ 7 Bohr. More precisely, the configurations, for the “Mo” and “S” atoms, have been adopted as $s3p2d1$ (cut-off radius, 7.0 Bohr) and $s2p2d1$ (cut-off radius, 7.04 Bohr) respectively. The k-points in the Monkhorst–Pack grid are set to $9 \times 9 \times 1$ for calculating the electronic properties of different unit cells. However, for obtaining the phonon dispersion we opt for the frozen phonon calculations with the k-points grid of $3 \times 3 \times 1$. The density mesh cut off is set to 90 Hartree. Furthermore, along the perpendicular direction (i.e., the normal to the plane), we provide sufficient vacuum to avoid the spurious interaction between periodic images.

Figures 1(a)–1(c) show the electronic band structures of the optimized unit cells of monolayer MoS₂ for the three distinct polytypes (2H, 1T, and 1T'). In order to optimize the geometries we have utilized the LBFGS (Limited-memory Broyden Fletcher Goldfarb Shanno) algorithm with the maximum stress tolerance value of 0.001 eV/\AA^3 . The structures are fully relaxed until the force on each atom becomes smaller than 0.01 eV/\AA .

For the 2H unit cell, the optimized in-plane lattice constants are obtained as, $a = b \simeq 3.19 \text{ \AA}$. On the other hand, the optimized lattice constants are $a = b \simeq 3.20 \text{ \AA}$ for the hexagonal 1T unit cell and $a \simeq 3.18 \text{ \AA}$, $b \simeq 5.75 \text{ \AA}$ and $c \simeq 18 \text{ \AA}$ for the triclinic 1T' unit cell. Moreover, for those fully relaxed

hexagonal and triclinic lattices, the “Mo”-“S” distances ($r_{\text{Mo-S}}$) have been calculated considering all the X, Y, and Z coordinates (as delineated in Figs. 1(a)–1(c)). For the monolayer MoS₂ with 2H phase, a direct bandgap of 1.7 eV has been computed at the “K” point of the Brillouin Zone (Fig. 1(a)). Besides, as shown in Fig. 1(b), the metallic 1T MoS₂ produces a bandstructure which is very much consistent with the other reported results.^{25,28} However, for the triclinic 1T', a negligible band opening of 0.016 eV has been observed near the Γ point (Fig. 1(c)) which is somewhat lesser than the DFT-PBE calculated value as reported in Ref. 35. The semiconducting 2H phase (having the “Mo” site in a trigonal prismatic coordination) provides most stable structure compared with the other polytypes.²⁸ In order to find the relative energetic stabilities of the 1T and 1T' phases (with octahedrally coordinated “Mo”), Putungan *et al.* calculated the energy per formula unit MX₂ (where, X = “S”, “Se”, “Te”) and suggested that the 1T' phase is always lower in energy by several hundreds of meV.²⁹ In a similar analysis,³⁶ Duerloo *et al.* performed the ground-state energy difference calculations (in the absence of mechanical stress) to show that the 1T' phases lie invariably below the 1T phases in energy (per MX₂ formula unit). Further to study the dynamical stability of the 2H, 1T, and 1T' phases, we employ DFT calculations and obtain the phonon dispersion curves. Figure 1(d) illustrates the phonon bandstructure of monolayer MoS₂ with 2H phase. In order to obtain the phonon dispersion curves, using frozen phonon calculations, we have formed the dynamical matrix of the system with a repetition of $9 \times 9 \times 1$.³⁷ Considering the phonon bandstructures obtained for the other two phases (Figs. 1(e) and 1(f)), we clearly see

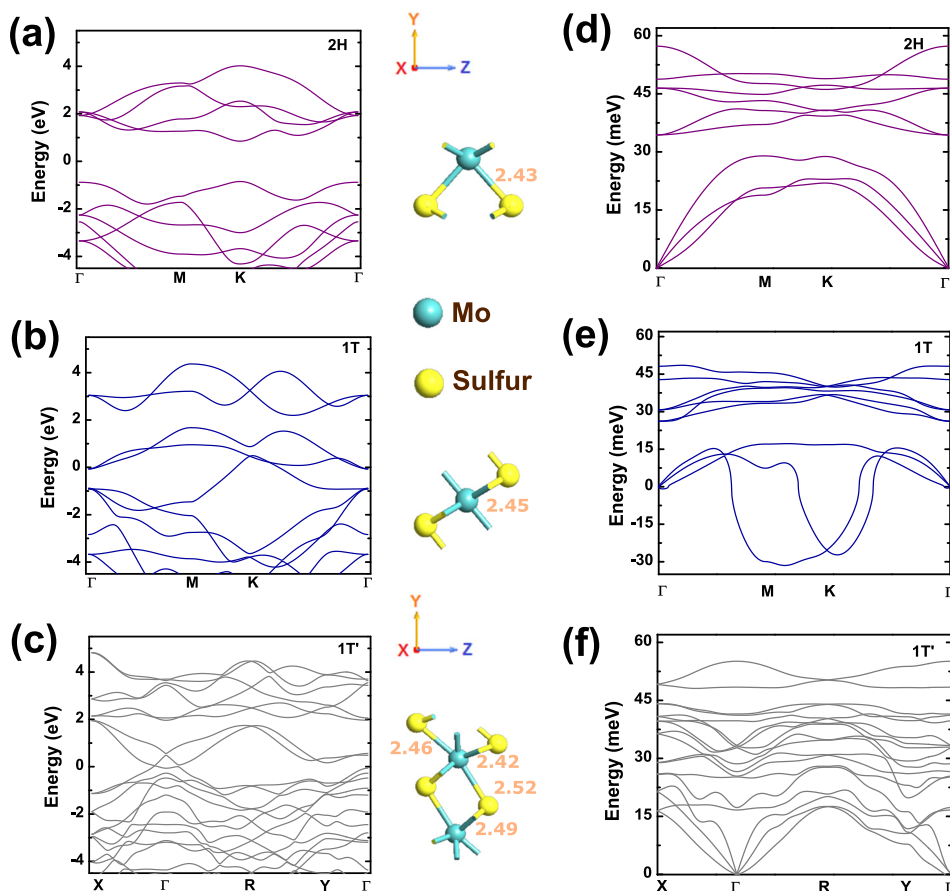


FIG. 1. Band structures of monolayer MoS₂ obtained for (a) 2H hexagonal, (b) 1T, and (c) triclinic 1T' lattices. Phonon dispersion curves for the three different polytypes are shown in (d), (e), and (f), respectively. Existence of negative frequencies in the phonon bandstructure of 1T phase indicates the structural instability of the material. The numbers marked in the unit cells denote the corresponding bond lengths in \AA .

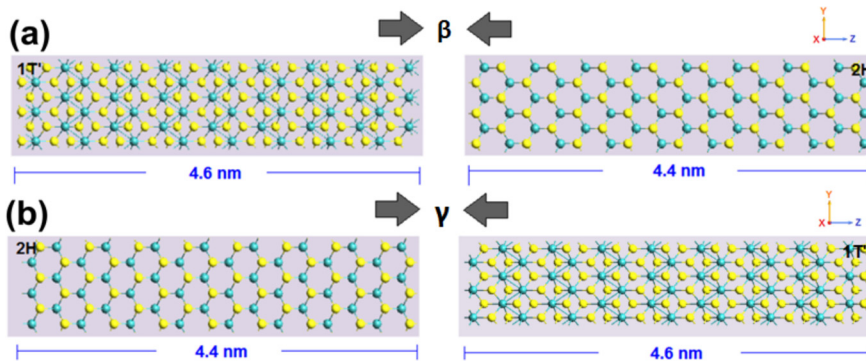


FIG. 2. Alignments of 2H and 1T' supercells used for modeling the planar hetero-phase structures, with (a) β and (b) γ phase boundaries. All the structures are periodic in the YZ plane.

the presence of imaginary or negative frequencies in the case of metallic 1T MoS₂. This confirms dynamical instability of the 1T phase. Hence, we adopt the 1T' crystal instead of 1T, for modeling the planar hetero-phase structures. In the following, we will demonstrate that even with 1T' polytype, the atomic arrangements and electronic structures of the metallic-to-semiconducting phase boundaries could be explained properly.

Aligning two large supercells of 2H and 1T' polytypes appropriately, we first try to model the β and γ phase boundaries (as shown in Fig. 2). For the composite structures of Figs. 2(a) and 2(b), the mean absolute strain values on the 2H sides as well as on the 1T' sides are calculated as 0.087% (with the individual components of strain tensor as, $\epsilon_{11} = \epsilon_{12} = 0\%$ and $\epsilon_{22} = 0.26\%$) and 0.043% (with $\epsilon_{11} = \epsilon_{12} = 0\%$ and $\epsilon_{22} = -0.13\%$), respectively. We then fully relax the combined supercells, using LBFGS algorithm (with maximum stress and force tolerance values ~ 0.001 eV/Å³ and 0.01 eV/Å, respectively), which considers all the possible translational and rotational movements to construct the final optimized geometries (which are in good agreement with experiential observations^{21,22}). The geometry optimized composite supercells (having dimensions 0.95 nm × 9.03 nm) finally form two distinct types of phase boundaries at the interfacing regions of 2H and 1T' planes (portrayed by the highlighted atoms in Fig. 3). Moreover, we find that the in-plane hetero-phase structure with the γ phase boundary is relatively more stable, than that with the β phase boundary. Compared with the hetero-phase structure with β phase boundary, the energy per atom value is ~ 0.0137 eV/atom lower in the case of the structure with γ phase boundary. The total energy per atom values for the geometry optimized composite supercells (each having 288

atoms) with β and γ phase boundaries are obtained as -857.1274 eV/atom and -857.1411 eV/atom, respectively. It is worth mentioning that we have swapped the axes here to make the Y-Z plane as the in-plane of the super cells, and consequently chosen the k-points in the Monkhorst–Pack grid as $1 \times 9 \times 9$ for calculating the different electronic properties. The Poisson solver is set with the periodic boundary conditions for the planes in X, Y, and Z directions.

The “Mo”–“Mo” distance at the β phase boundary is calculated as 2.76 Å; whereas the Z-distance between “Mo”–“Mo” atoms at the γ phase boundary is found to be 2.52 Å. Perhaps, the slight differences in the “Mo”–“Mo” distances at the boundaries might have originated from the choice of our unit cells, lattice constants. However, it is important to realize here that the phase transformation in monolayer MoS₂ is a complex dynamic process which incorporates various states such as, formation of the precursor phase, migration of the individual phase boundaries, and of course gliding of the atomic planes.²¹ Furthermore, any presence of spontaneous ripples in the monolayer MoS₂ can make the phase transition between 1T' and 2H unfavorable.³⁶ For such a case, we may have to apply some additional strain.³⁶

These optimized combined supercells are then used to calculate the electronic structures. To understand the electronic properties and charge carrier transport at the phase boundaries we define three different regions across the Y-Z plane (Fig. 3): one situating exactly at the phase boundary (marked as Int_r); and the other two are deep inside the 2H and 1T' regions (labeled as 2H_r and 1T'_r, respectively). Figure 4 shows the projected density of states (DOS) plots for the atoms within the 2H_r, Int_r, and 1T'_r regions. It is evident that the DOS of Int_r regions resemble more with the 1T'_r regions, regardless of the type of the phase boundary (Figs. 4(a) and 4(b)).

We further study the force distribution across the two phase boundaries, as it might be helpful to understand the nature of DOS distribution along the length of the composite supercells. Since the forces are the vectors spread in three dimensions, thereby depending upon the distribution of the force components, the organization of DOS can be very sparse.³⁸ As shown in Fig. 5, the length of the arrows are showing the magnitude of the force components acting on atoms, whereas the arrow heads are actually denoting the directions in X-Y-Z plane. Though the force components acting on the atoms around the β phase boundary are somewhat larger in magnitude, those are almost equally distributed

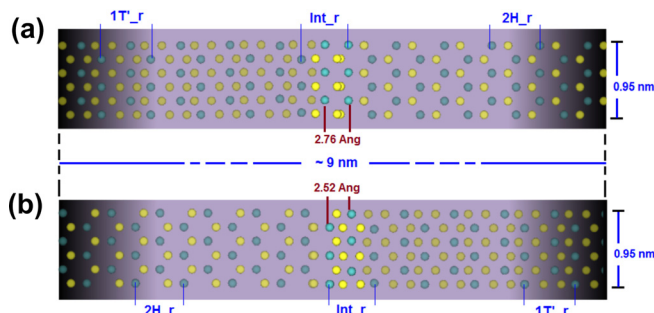


FIG. 3. Atomistic models of the in-plane hetero-phase structures with (a) β and (b) γ phase boundaries. For both the optimized planar structures (in YZ plane), we have the distinct phase transition regions.

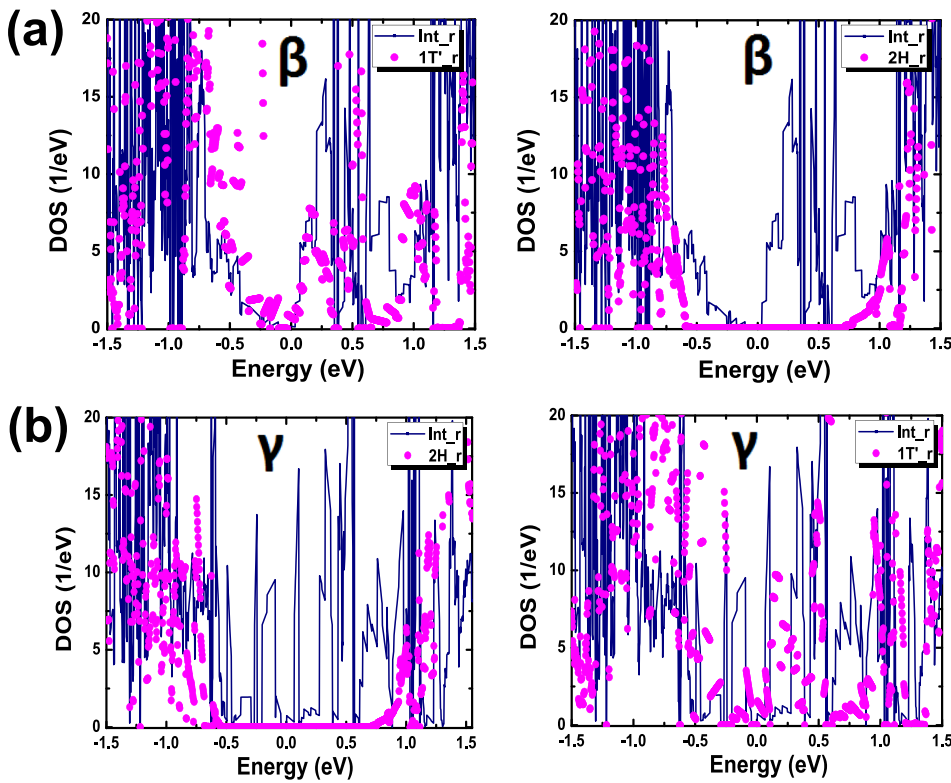


FIG. 4. Projected density of states (DOS) plots, considering the atoms located in the $1T'_r$, Int_r , and $2H_r$ regions of the hetero-phase structures with (a) β and (b) γ phase boundaries.

across the entire plane (Fig. 5(a)). On the contrary, we see that the forces acting on atoms of the hetero-phase structure with γ phase boundary are very much localized in the phase transition and $1T'$ regions (Fig. 5(b)). For the purpose of meaningful illustration of the forces acting on atoms of both the structures, we opt for a threshold of 0.05 eV/\AA along with the scaling factor of “1.”

Now, to investigate the charge carrier transfer through the β and γ phase boundaries, we have converted the optimized hetero-phase structures of Figs. 3(a) and 3(b) into the two port device structures. The lengths of the semi-infinite electrodes are taken as 5.75 \AA and 5.53 \AA (formed extending the $1T'$ and $2H$ ends respectively). In order to calculate the transmission along the channels of the two port devices, we use NEGF formalism along with DFT calculation.³⁹ For solving the Poisson’s equation, we use Dirichlet boundary condition in the transport direction (Z direction), and periodic boundary conditions in the other (X and Y directions). We select the lower bound and the circle points of contour integral as 3 Hartree and 60, respectively. The k-points in the Monkhorst–Pack grid are set to $1 \times 9 \times 99$.

Figure 6 shows the energy-position resolved local density of states diagrams and the transmission spectra of the

two port device structures. Hereafter, we will refer the devices with the central regions formed of the hetero-phase structures having the β and the γ phase boundaries as the β -device and the γ -device, respectively. Moreover, it is important to mention here that, in this study the energy zero is represented as the position of the Fermi level (E_F). Now, as depicted in Figs. 6(a) and 6(b), there are sharp changes in local density of states (LDOS) which take place exactly around phase boundaries, and abruptly isolates the metallic phase from the semiconducting phase. The most interesting aspects of these devices are the $1T'$ extensions which will help to achieve excellent impedance matching with various metal contacts, while keeping the semiconducting properties of $2H$ region unscathed. We also find that the Schottky barrier height is different for these two phase boundaries. For the β -device we find that the barrier heights for both types of charge carriers are almost same ($\sim 0.8 \text{ eV}$), whereas the phase boundary of the γ -device delineates a classical p-type Schottky barrier of $\sim 0.68 \text{ eV}$. The difference in electrical nature of the γ phase boundary might have emerged from the effect of non-uniformly distributed force components across the plane (as shown in Fig. 5(b)). Besides, Figs. 6(c) and 6(d) delineate the up-spin components of transmission spectra (obtained at zero bias) of the β -device and the γ -device, respectively. Considering the energy range of 0 eV to 5 eV , we find that the transmission is somewhat larger in the γ -device (although for the negative energy values, transmission in both the devices is similar). Further, it could be inferred that, while β boundary might yield similar performances for both p and n-type MOS transistor operations, the γ boundary will provide lower threshold voltage for p-type devices.

In summary, we have developed atomistic models for the planar hetero-phase structures of monolayer MoS_2 , having two disparate phase transition regions (β and γ) which

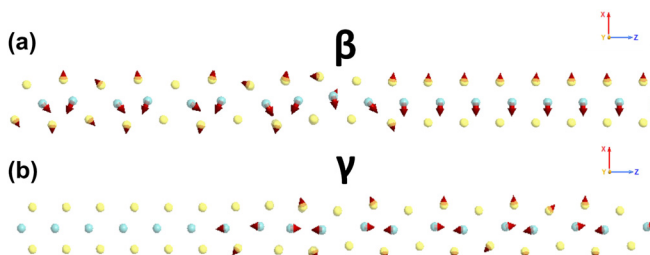


FIG. 5. Distribution of the force components in the hetero-phase structures with (a) β and (b) γ phase boundaries.

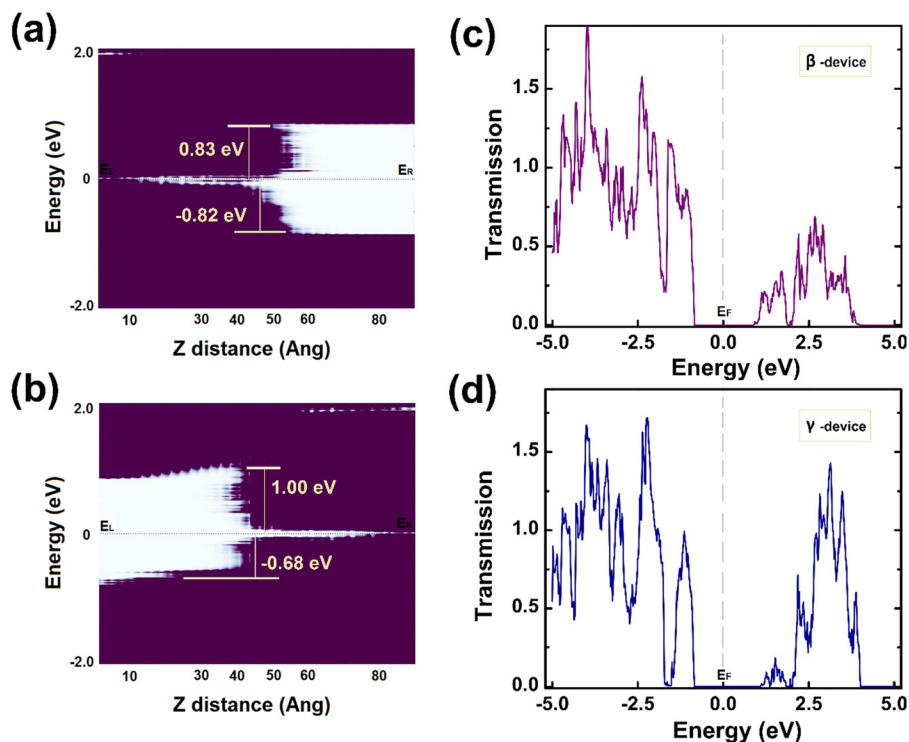


FIG. 6. Energy-position resolved LDOS diagrams for the (a) β -device and (b) γ -device plotted considering a small energy range of -2.0 eV to 2.0 eV. The axes labeled as “Z distance” are denoting the lengths of the channel regions (in real space). The minimum and maximum values of the device density of states (in $1/\text{eV}$) are opted as 0 and 0.05, respectively. In the LDOS plots, thus the white regions are devoid of any states. At equilibrium, $E_L = E_R = E_F$ (i.e., the Fermi levels of the left electrode, the right electrode, and the central region are all aligned). The zero bias transmission spectra of the β -device and the γ -device are portrayed in (c) and (d), respectively.

are in good agreement with experimental results. We employed NEGF formalism to estimate the transmission and LDOS and to evaluate the Schottky barrier nature of the phase boundaries. Our study reveals that the γ boundary yields p-type Schottky barrier (~ 0.68 eV), whereas the β boundary leads to symmetric Schottky barrier of ~ 0.8 eV.

This work was supported by the SERB, Department of Science and Technology (DST), Government of India, under Grant No. SB/S3/EECE/0209/2015.

¹B. Radisavljevic, A. Radenovic, J. Brivio, V. Giacometti, and A. Kis, *Nat. Nanotechnol.* **6**, 147–150 (2011).
²F. Schwierz, *Nat. Nanotechnol.* **5**, 487–496 (2010).
³S. Das and J. Appenzeller, *Appl. Phys. Lett.* **103**, 103501 (2013).
⁴T. Roy, M. Tosun, M. Hettick, G. H. Ahn, C. Hu, and A. Javey, *Appl. Phys. Lett.* **108**, 083111 (2016).
⁵K. Alam and R. Lake, *IEEE Trans. Electron Devices* **59**, 3250–3254 (2012).
⁶Y.-C. Lin, C.-Y. S. Chang, R. K. Ghosh, J. Li, H. Zhu, R. Addou, B. Diaconescu, T. Ohta, X. Peng, N. Lu, M. J. Kim, J. T. Robinson, R. M. Wallace, T. S. Mayer, S. Datta, L.-J. Li, and J. A. Robinson, *Nano Lett.* **14**(12), 6936–6941 (2014).
⁷P. Miró, M. Audiffred, and T. Heine, *Chem. Soc. Rev.* **43**, 6537–6554 (2014).
⁸D. Saha and S. Mahapatra, *J. Appl. Phys.* **119**, 134304 (2016).
⁹K. F. Mak, C. Lee, J. Hone, J. Shan, and T. F. Heinz, *Phys. Rev. Lett.* **105**, 136805 (2010).
¹⁰N. R. Pradhan, D. Rhodes, Q. Zhang, S. Talapatra, M. Terrones, P. M. Ajayan, and L. Balicas, *Appl. Phys. Lett.* **102**, 123105 (2013).
¹¹H. Wang, L. Yu, Y.-H. Lee, Y. Shi, A. Hsu, M. L. Chin, L.-J. Li, M. Dubey, J. Kong, and T. Palacios, *Nano Lett.* **12**, 4674–4680 (2012).
¹²J. Kang, W. Liu, D. Sarkar, D. Jena, and K. Banerjee, *Phys. Rev. X* **4**, 031005 (2014).
¹³I. Popov, G. Seifert, and D. Tomànek, *Phys. Rev. Lett.* **108**, 156802 (2012).
¹⁴J. Kang, W. Liu, and K. Banerjee, *Appl. Phys. Lett.* **104**, 093106 (2014).
¹⁵C. Gong, L. Colombo, R. M. Wallace, and K. Cho, *Nano Lett.* **14**, 1714–1720 (2014).

¹⁶M. S. Choi, D. Qu, D. Lee, X. Liu, K. Watanabe, T. Taniguchi, and W. J. Yoo, *ACS Nano* **8**, 9332–9340 (2014).
¹⁷Y. Du, L. Yang, J. Zhang, H. Liu, K. Majumdar, P. D. Kirsch, and P. D. Ye, *IEEE Electron Device Lett.* **35**(5), 599–601 (2014).
¹⁸N. Kaushik, D. Karmakar, A. Nipane, S. Karande, and S. Lodha, *ACS Appl. Mater. Interfaces* **8**, 256–263 (2016).
¹⁹R. Kappera, D. Voiry, S. E. Yalcin, B. Branch, G. Gupta, A. D. Mohite, and M. Chhowalla, *Nat. Mater.* **13**, 1128–1134 (2014).
²⁰G. Eda, T. Fujita, H. Yamaguchi, D. Voiry, M. Chen, and M. Chhowalla, *ACS Nano* **6**, 7311–7317 (2012).
²¹Y.-C. Lin, D. O. Dumcenco, Y.-S. Huang, and K. Suenaga, *Nat. Nanotechnol.* **9**, 391–396 (2014).
²²Supplementary Information in Doi: [10.1038/NNANO.2014.64](https://doi.org/10.1038/NNANO.2014.64), Available at <http://www.nature.com/>, Nature Nanotechnology.
²³Y.-C. Lin and K. Suenaga, National Institute of Advanced Industrial Science and Technology, Japan, private communication (2015).
²⁴D. Voiry, A. Goswami, R. Kappera, C. Silva, D. Kaplan, T. Fujita, M. Chen, T. Asefa, and M. Chhowalla, *Nat. Chem.* **7**, 45–49 (2015).
²⁵G. Gao, Y. Jiao, F. Ma, Y. Jiao, E. Waclawik, and A. Du, *J. Phys. Chem. C* **119**, 13124–13128 (2015).
²⁶K. C. Santosh, C. Zhang, S. Hong, R. M. Wallace, and K. Cho, *2D Mater.* **2**, 035019 (2015).
²⁷Z. Hu, S. Zhang, Y.-N. Zhang, D. Wang, H. Zeng, and L.-M. Liu, *Phys. Chem. Chem. Phys.* **17**, 1099–1105 (2015).
²⁸M. Calandra, *Phys. Rev. B* **88**, 245428 (2013).
²⁹D. B. Putungan, S.-H. Lin, and J.-L. Kuo, *Phys. Chem. Chem. Phys.* **17**, 21702 (2015).
³⁰B. Ouyang, G. Lan, Y. Guo, Z. Mi, and J. Song, *Appl. Phys. Lett.* **107**, 191903 (2015).
³¹See <http://quantumwise.com/> for QuantumWise Atomistix ToolKit (ATK) with Virtual NanoLab.
³²J. P. Perdew, K. Burke, and M. Ernzerhof, *Phys. Rev. Lett.* **77**(18), 3865 (1996).
³³T. Ozaki, *Phys. Rev. B* **67**, 155108 (2003).
³⁴T. Ozaki and H. Kino, *Phys. Rev. B* **69**, 195113 (2004).
³⁵X. Qian, J. Liu, L. Fu, and J. Li, *Science* **346**, 1344 (2014).
³⁶K.-A. N. Duerloo, Y. Li, and E. J. Reed, *Nat. Commun.* **5**, 4214 (2014).
³⁷D. Saha and S. Mahapatra, “Analytical insight into the lattice thermal conductivity and heat capacity of monolayer MoS_2 ,” *Phys. E* (in press).
³⁸P. T. Metzger, *Phys. Rev. E* **70**, 051303 (2004).
³⁹M. Brandbyge, J.-L. Mozos, P. Ordejón, J. Taylor, and K. Stokbro, *Phys. Rev. B* **65**, 165401 (2002).